NMR solution conformation of heparin-derived hexasaccharide

Dmitri MIKHAILOV*, Robert J. LINHARDT† and Kevin H. MAYO*[1]

*Departments of Biochemistry, Biomedical Engineering Center, 4-225 Millard Hall, University of Minnesota Health Science Center, 435 Delaware Street, S.E., Minneapolis, MN 55455, U.S.A., and †Division of Medicinal and Natural Products Chemistry and Department of Chemical & Biochemical Engineering, PHAR S328, The University of Iowa, 115 S. Grand Ave., Iowa City, Iowa 52242, U.S.A.

The solution conformation of homogeneous, heparin-derived hexasaccharide (residues A, B, C, D, E, F) has been investigated by using ^{1}H-NMR spectroscopy. Intra-ring conformations have been defined by *J*-coupling constants and inter-proton nuclear Overhauser effects (NOEs), and the orientation of one ring with respect to the other has been defined by inter-ring NOEs. NOE-based conformational modelling has been done by using the iterative relaxation matrix approach (IRMA), restrained energy minimization to refine structures and to distinguish between minor structural differences and equilibria between various intra-ring forms. All glucosamine residues B, D and F are in the $^4C_1$ chair conformation. The uronate (A) residue is mostly represented by the $^1H_2$ form, whereas internal iduronates (C and E) exist in equilibrium between the chair and skewed boat forms. Deviations in some NOEs indicate a minor contribution of the $^2H_1$ form to the A ring. Glycosidic dihedral angles, which define the overall oligosaccharide conformation, were further refined by combining *in vacuo* energy map calculations and restrained energy minimization in explicit solvent water. Conformational stability was further assessed by subjecting NOE and IRMA-derived structures to 600 ps of unrestrained molecular dynamics in explicit solvent.

INTRODUCTION

Heparin is mainly a polydisperse sulphated copolymer of 1→4-linked glucosamine and uronic acid residues. Most of the heparin molecule is accounted for by this repeating disaccharide unit that consists primarily of 2-O-sulphated α-L-idopyranosyluronic acid (IdoA) 2-sulphate and 2-deoxy-2-sulphamido-α-D-glucopyranose ($GlcNSO_3$) 6-sulphate [1,2], although both β-D-glucopyranosyluronic acid and α-L-idopyranosyluronic acid residues are also found. This repeating sequence represents at least 85% of heparins from beef lung and about 75% of those from intestinal mucosa [3]. The balance of the molecule is constituted largely of residues of 2-acetamido-2-deoxy-D-glucopyranose and D-glucopyranosyluronic acid, although their modes of bonding and distribution within the polymer, as well as their degrees of sulphation, have yet to be established unequivocally. Occasionally 6-desulphated and/or 2-N-acetylated residues are also present. In general, the overall conformation of heparin can be described by a set of glycosidic bond dihedral angles. The problem of measuring precise values for glycosidic dihedral angles as well as the degree of flexibility around glycosidic bonds in polysaccharides has been addressed (for example in [4]). Experimental approaches based on the measurement of NMR coupling constants [5] or chemical shifts [6] usually lack precision, whereas angles derived theoretically that have been obtained from energy calculations must be viewed with caution owing to their force-field dependence. Moreover, the use of experimentally determined restraints during energy minimization can result in the formation of 'virtual conformers' [7], molecular conformations that are not at the global energy minimum.

One way to approach the problem of better understanding the solution conformation of long-chain heparin is to perform structural studies on homogeneous, short-chain heparin-derived oligosaccharides as models for the longer heparin polymer. Isolation and chemical composition of the most common hexasaccharide repeat unit in heparin has been reported [8,9]: ΔUA2S(1→4)-α-D-GlcN*p*-S6S(1→4)-α-L-IdoA*p*-2S(1→4)-α-D-GlcN*p*-S6S-α-L-IdoA*p*-2S(1→4)-α-D-GlcN*p*-S6S. The chemical structure of this hexasaccharide is shown in Figure 1 with residues labelled A to F. ^{1}H-NMR assignments have been made for this hexasaccharide [10] as well as for various other heparin-derived oligosaccharides [11,12]. However, little is known about the details of the solution conformation of these oligosaccharides prepared via heparin depolymerization, that produces, at the non-reducing end, a terminal uronate with an unsaturated 4,5 carbon bond. For di- and oligosaccharides, which have been studied by NMR, proton coupling constants for this terminal uronate indicate conformational flexibility [8,13]. Crystallographic data show that this residue exists in two different forms ($^2H_1$ and $^1H_2$) (Scheme 1) within the same unit cell, indicating that these two forms are nearly equi-energetic [14]. The non-terminal α-L-idopyronosyluronate residue is likewise internally flexible, whereas the 2-deoxy-2-aminoglucopyranose and β-D-glucopyranosyluronate residues are conformationally rigid in solution [15,16]. Although derivation of the conformation of iduronate-containing polysaccharides and oligosaccharides is complicated by conformational equilibria within their iduronate pyranose rings, the possibilities in phase space are limited because only two conformations, $^1C_4$ chair and $^2S_0$ skewed boat (Scheme 1), are energetically favourable [15,17]. This flexibility within α-L-idopyranosyluronate residues might contribute to unique binding properties of heparin, thereby affording additional versatility and biological activity. Other glycosaminoglycans having approximately the same molecular mass and degree of sulphation,

Abbreviations used: 2D, two-dimensional; FGF, fibroblast growth factor; IdoA, idopyranosyluronic acid; IRMA, iterative relaxation matrix approach; MD, molecular dynamics; NOE, nuclear Overhauser effect; NOESY, NOE spectroscopy; NPT, constant **n**umber of particles, constant **p**ressure and constant **t**emperature statistical ensemble; NVT, constant **n**umber of particles, constant **v**olume and constant **t**emperature statistical ensemble; RMS, root-mean-square; RMSD, RMS deviation; TPPI, time proportional phase incrementation.

[1] To whom correspondence should be addressed.

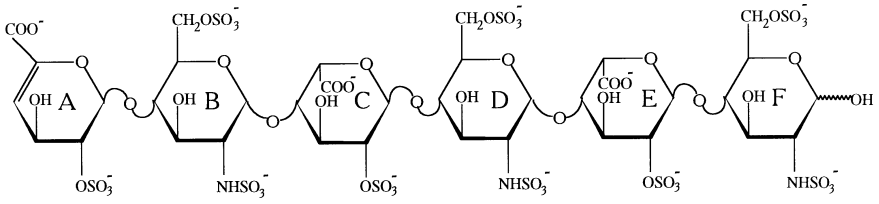

Figure 1 Chemical structure of heparin-derived hexasaccharide

Residues are labelled A, B, C, D, E and F for uronate, glucosamine, iduronate, glucosamine, iduronate and glucosamine rings respectively, as discussed in the text. Note that ring A uronate has an unnatural double bond resulting from heparinase digestion.

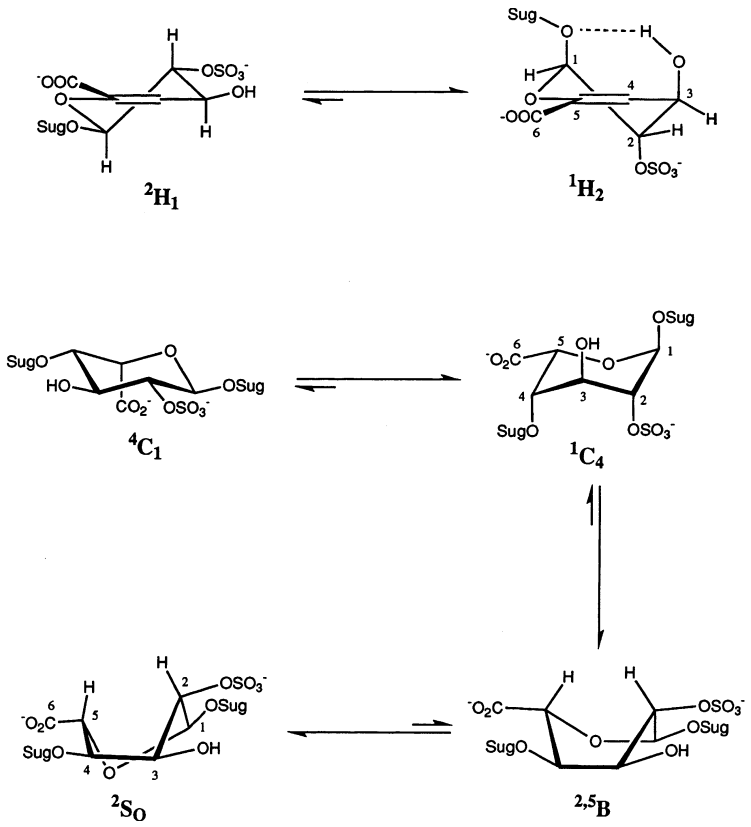

Scheme 1 Possible ring conformations of uronate (ring A) and iduronate (rings C and E) in the hexasaccharide, depicted as discussed in the text

but containing the more rigid β-glucopyranosyluronate residues, show considerably less biological activity. In addition, the positions of sulphate groups seem to have a role in glycosaminoglycan activity. For example, fibroblast growth factor 2 (FGF-2) binds avidly to a heparin hexasaccharide composed of three consecutive -IdoA(2-OSO_3)-GlcNSO_3(6-OSO_3) disaccharide units [18,19]. However, binding studies involving chemically modified heparin preparations suggest that whereas the glucosamine *N*-sulphate and iduronate 2-*O*-sulphate groups are essential for this interaction, the glucosamine 6-*O*-sulphates are redundant [19–21]. The X-ray crystal structure of heparin hexasaccharide complexed with FGF-2 confirms the importance of these two sulphate groups [22]. In contrast, binding of hepatocyte growth factor to heparin/heparan sulphate seems to depend primarily on glucosamine 6-*O*-sulphate groups [23]. The conformation of methyl-*O*-sulphate groups is therefore of interest in understanding heparin–protein interactions involving the sulphate group at this position.

The present study is aimed at determining the solution conformation of heparin-derived hexasaccharide by using ^{1}H-NMR nuclear Overhauser effects (NOEs) and coupling constants, relaxation rates, the iterative relaxation matrix approach (IRMA), restrained energy minimization and molecular dynamics (MD). This work is a continuation of structural studies initiated with heparin-derived tetrasaccharide [24]. The presence of an additional disaccharide repeat unit raises the molecular complexity closer to that of larger heparin fragments and permits the derivation of more information about glycosidic dihedral angles, which define the overall shape of the heparin oligosaccharide. Although working with heterogeneous fractions of higher-molecular-mass heparins presents many problems from the experimental perspective, the use of homogeneous fractions

of small heparin-derived oligosaccharides allows one to determine experimentally a number of reliable conformational parameters essential for understanding and modelling the structure of larger heparin molecules. Thus studying the hexasaccharide provides a better structural model for longer heparin molecules.

MATERIALS AND METHODS

Heparin hexasaccharide isolation

Approximately 1 g of heparin was dissolved in 100 ml of distilled water and dialysed exhaustively, freeze-dried and prepared at exactly 20 mg/ml in distilled water [25]. To 50 ml of heparin (20 mg/ml) was added 5 ml of sodium phosphate buffer [5 mM sodium phosphate (pH 7)/200 mM NaCl] containing 100 m-units of heparinase. The reaction mixture was incubated at 30 °C for 48 h. Under these conditions, 30 % of the heparinase-cleavable linkages are broken, giving rise to the maximum possible amount of the desired hexasaccharide product. The reaction was terminated by heating to 100 °C for 5 min and the depolymerization mixture was fractionated by gel filtration and strong anion-exchange HPLC as described previously [26].

NMR measurements

For NMR measurements, 2 mg of freeze-dried heparin hexasaccharide was dissolved in 0.5 ml of ^2H_2O. The pH was adjusted to the desired value by adding microlitre quantities of NaO^2H or ^2HCl to the sample. The salt concentration was adjusted to 1 mM. For most experiments, the temperature was controlled at 5 °C to effect shorter relaxation rates and to minimize the contribution from high-energy conformations. ^{1}H-NMR spectra were acquired on a Bruker AMX-600 NMR spectrometer operating at a ^{1}H frequency of 600 MHz.

For ^{1}H resonance assignments, two-dimensional (2D) NMR homonuclear magnetization transfer (HOHAHA) spectra, obtained by spin-locking with an MLEV-17 sequence [27] with a mixing time of 60 ms, were used to identify spin systems. NOE spectroscopy (NOESY) experiments [28,29] were performed for mixing times of 100, 200, 300, 500 and 700 ms to connect saccharide ring-spin systems sequentially and to define NOE build-up curves for use in IRMA calculations described below. Relative chemical shifts for 6*S* and 6*R* protons were assumed to be the same as for heparin-derived tetrasaccharide [24]. ^{1}H–^{1}H coupling constants were taken from previous work on the same hexasaccharide [10]. 2D-NMR data were acquired in the phase-sensitive mode by using TPPI (time proportional phase incrementation) or States–TPPI [30–32]. The residual water resonance was suppressed by direct irradiation (0.6 s) during the relaxation delay between scans. Spectra were normally collected as 256–512 t_1 experiments each with 2048 complex data points and 96 scans over a spectral width of 5 kHz in both dimensions with the carrier placed on the water resonance. 2D-NMR spectra were processed off-line on an SGI Indigo Extreme workstation with the Felix program (Biosym/MSI, San Diego, CA, U.S.A.). Free induction decays were generally zero-filled to 2048 in the t_1 dimension and SS apodized before Fourier transformation. ^{1}H spin–lattice relaxation times (T_1) were measured by using the inversion recovery method with water suppression. T_1 values were calculated by using the program XSPEC (Bruker Instruments, Billerica, MA, U.S.A., and Spectrospin AG, Zurich, Switzerland).

Molecular modelling

Initial hexasaccharide structures were taken from the Brookhaven PDB structural database and modified by introducing a double bond at the C-4/C-5 position of the non-reducing uronate ring by using the InsightII program (Biosym/MSI). The AMBER forcefield with Homans additions for saccharides [33] was used in all calculations. Parameters for sulphates were taken from *ab initio* calculations [34], and parameters for hydrogen bonds between carbohydrate hydroxy hydrogens and oxygens and water were taken from Glennon et al. [35]. The total molecular charge was set to -12 (the number of charged groups at pH 6). Partial charges for sulphates were taken as reported by Huige and Altona [34] with slight adjustments so that the total charge of every residue was equal to -2. Optimization of the A ring conformation included an initial steepest descent minimization, followed by 1 ps MD and conjugated gradient minimization until the derivative was less than 0.01. Owing to the presence of iduronate ring interconversions, an ensemble of four possible hexasaccharide structures (various combinations of chair and boat forms for internal iduronate rings C and E) was constructed and was used in all subsequent calculations.

NOE build-up curves (mixing times of 100, 200, 300, 500 and 700 ms) were analysed to check for possible indirect magnetization transfer pathways (spin diffusion), and NOE cross-peak intensities were calculated by using the IRMA [36,37] with ensemble-averaging through the NMR-Refine program (Biosym/MSI) on an SGI Indigo Extreme workstation. The overall rotational correlation time used in IRMA simulations was estimated from the value reported for a heparin pentasaccharide [38]. In the hexasaccharide, the additional ring increases the mass and the length of the oligosaccharide proportionally, but modifies the transverse dimensions only slightly. Perpendicular and parallel components for the symmetric top diffusion tensor for the hexasaccharide were estimated to be 6/5 and $(6/5)^3$, respectively, relative to those for the pentasaccharide. Using the length and breadth of an extended oligosaccharide, symmetrical top rotational correlation times ranged from 1.2 to 2.2 ns. A single isotropic overall tumbling correlation time of 1.6 ns was obtained as an average for all possible proton pairs within a distance cutoff of 4 Å. Although this represents a rather crude estimate with an error of approx. 30 %, the effect of this error on IRMA-derived inter-proton distances is considerably less owing to the r^{-6} weighting factor. Furthermore internal ring mobilities were not considered because previous studies showed large motional order parameters (highly restricted motions) for analogous heparin-derived oligosaccharides [24,38]. In this respect, rigid-body isotropic tumbling provides a reasonable motional model from which to calculate interproton distances.

The leakage rate for diagonal peaks was calculated as the difference between the experimental relaxation rate and the theoretical dipole–dipole relaxation rate for the same proton pair averaged over all structures in the conformational ensemble. Owing to signal overlap, only well-resolved peaks located in different parts of the oligosaccharide were chosen to estimate a three-peak (B2, D2, F1) average leakage rate of 0.1 s^{-1}, which was used in IRMA calculations. Even though different chemical environments can lead to different leakage rates for different protons in different parts of a molecule, this approximation was deemed acceptable, particularly at short mixing times and given the small size of the hexasaccharide. Relaxation matrix elements were averaged with the NOE volume as the weighting function to provide adequate averaging over longer mixing times. Symmetry-related NOESY cross-peaks were volume-integrated and averaged. A total of 32 NOE cross-peaks, measured at five mixing times, were used as input for IRMA calculations. Six NOEs, B2–B4, B3–B5, D2–D4, D3–D5, F2–F4 and F3–F5, were taken as references for calculating relaxation matrix elements. With glucosamines in a $^4C_1$ chair conformation, these inter-proton

NOEs provide good distance calibrations. Furthermore the use of NOEs from both B and D (internal) and F (terminal) rings to calibrate distances helps to average out internal motional differences. The set of distance constraints was calculated on the basis of an r^{-6} average for the ensemble of structures with an overall correlation time of 1.6 ns and assuming slow (10^4–10^6 s^{-1}) interconversion between different ring conformers [39]. This averaging approach reflects the fact that experimental NOEs represent a time average over a number of conformations.

Direct NOE volume refinement [40] was used for five sets of overlapped peaks: A1–A3 (B6R), B(D)H4–B(D)H6R; B(D)H6R–B(D)H6S; B(D)H4–B(D)H5; C(E)H1–C(E)H2. Dihedral angle constraints were derived from coupling constants by using the Haasnoot equation [41]. Structures were then minimized for 10000 cycles by the conjugate gradient method until the derivative was less than 0.01 with a variable force constant of 3–60 kcal/mol per Å^2 for distance constraints and a force constant of 3 kcal/mol per deg^2 for dihedral angle constraints. The maximum distance force constant defines the restraint energy equal to kT_{300K} when the distance violation is 0.05 Å and the dihedral angle violation is 10 °. For simulations *in vacuo*, a distance-dependent dielectric constant $4r$ without cutoffs was used to partly account for the absence of solvent. This ensemble of structures was then used as an input in subsequent IRMA cycles with the same motional parameters to update the set of distance constraints.

To measure the quality of IRMA-calculated structures, *R*-factors, which compare experimental data and model structures, were used. The definition of the NMR *R*-factor used here is analogous with that used by Gonzales et al. [42]:

$$R = \frac{\sum_{\tau_m}\sum_{i} \tau_m \,|\, A_i^t(\tau_m) - A_i^e(\tau_m) \,|}{\sum_{\tau_m}\sum_{i} \tau_m \,|\, A_i^e(\tau_m) \,|} \qquad (1)$$

where A_i are cross-peak intensities and τ_m are mixing times. Convergence usually occurred within five IRMA cycles. The resulting ensemble represents 'virtual' conformations of the hexasaccharide that often differ from the global minima owing to applied restraints. To test the sensitivity of the overall conformation to the restraint energy, structures were recalculated with larger distance force constants: K_{dis} = 3, 15, 30 or 60 kcal/mol per Å^2.

Because this hexasaccharide is highly negatively charged, structural refinement was performed in the presence of solvent water molecules and counterions. Simulations of smaller and less charged saccharides have been done previously [4,43–45]. Structures obtained by using the IRMA protocol with K_{dis} = 60 kcal/mol per Å^2 were used as inputs for explicit solvent simulations. Sodium counterions were placed 2.5 Å away from sulphates and carboxylates to neutralize negatively charged groups. Molecules were then solvated in a 42 Å × 23 Å × 23 Å water box with the number of water molecules varying from 669 to 676 depending on the hexasaccharide structure used. Assemblies were then equilibrated within the solvent box by using short conjugated gradient minimizations for 1000 steps to remove bad contacts, followed by 30 ps of NPT (constant **n**umber of particles, constant **p**ressure and constant **t**emperature statistical ensemble) MD at 300 K and 1.0 bar of pressure. The system was equilibrated in a thermal bath with a coupling constant of 0.5 ps, and the pressure of the system was controlled by isotropically coupling atomic positions and the size of the cell to a pressure bath with a relaxation constant of 0.5 ps. The energy of the system stabilized within the first 20 ps. As is typical of NPT dynamics, large pressure fluctuations (within ±500 bar) were observed during these runs, and the size of the box decreased to about 36 Å × 20 Å × 20 Å, indicating the initial low internal pressure of the system. During simulations, positional restraints of 50 kcal/mol per Å were applied for all atoms along with the NMR-derived restraints with K_{dis} = 60 kcal/mol per Å^2 and K_{dih} = 3 kcal/mol per rad^2. Without these positional restraints, structures became highly distorted during equilibration. Positional restraints were then gradually removed by decreasing the force constant by 10 kcal/mol per Å during each of the five subsequent 500-step conjugated gradient minimizations. The resulting system was minimized first with and then without NMR-derived restraints (no positional restraints were applied) until the root-mean-square (RMS) value was less than 0.01. Structures minimized without restraints were then used as input for unrestrained MD. These were subjected to 10 ps of NPT dynamics including positional restraints (same parameters as above), which were then gradually removed during a subsequent 10 ps of NPT dynamics. Because pressure control can introduce artifacts into an MD trajectory, productive runs were initiated for the NVT (constant **n**umber of particles, constant **v**olume and constant **t**emperature statistical ensemble). As judged by observing the total energy, equilibration of the system was reached within 80 ps of the NVT simulation, making the total equilibration time 100 ps. Conformational parameters were analysed from the subsequent 500 ps of simulation. A dielectric constant of 1 and a cutoff of 9 Å were used throughout the explicit solvent simulations. Charge groups were implemented to decrease the artifacts arising from use of electrostatic energy cutoffs.

RESULTS AND DISCUSSION

For heparin-derived hexasaccharide, the six sugar rings are identified as A, B, C, D, E and F from the non-reducing end to the reducing end (Figure 1). ^{1}H resonance spin systems have been non-specifically assigned to glucosamine and uronate rings [10], based primarily on chemical shifts [11] with 2D-NMR correlated spectroscopy data. In the present study these groupings have been confirmed with total correlation spectra, and sequence-specific resonance assignments have been made by identifying inter-residue H1–H4 NOE connectivities as shown in Figure 2.

Coupling constants obtained from analysis of one-dimensional ^{1}H-NMR and 2D double-quantum-filtered correlated spectroscopy spectra indicate that all three 2-deoxy-2-*N*-sulpho-α-D-glucosamine-6-sulphate (referred to simply as glucosamine) residues B, D and F maintain the $^4C_1$ conformation (Scheme 1), as suggested for glucosamine rings in parent heparin and in other heparin-derived oligosaccharides [15,16,24,46,47]. Small H1 and H2 coupling constants ($^3J_{1,2}$ = 3.4–3.5 Hz) indicate an axial–equatorial relationship between H1 and H2 protons, whereas larger $^3J_{i,j}$ values (more than 9Hz) for H3, H4 and H5 indicate a *trans*-diaxial relationship between these protons. The $^4C_1$ chair form is further supported by NOE-based conformational modelling discussed below. Moreover, these data indicate that neither the unsaturated uronate nor iduronate residues substantially modify this glucosamine ring conformation. This is consistent with the observation that the $^4C_1$ glucosamine (3-O-sulphated 2-deoxy-2-*N*-sulpho-α-D-glucosamine-6-sulphate ring) ring conformation is also unperturbed by adjacent β-D-glucuronate and 2-O-sulphated α-L-iduronate residues in a pentasaccharide corresponding to the ATIII binding site in heparin [47]. A similar finding also has been made with a heparin-derived tetrasaccharide [24]. These data suggest that increasing the length of the heparin chain seems not to change the overall glucosamine ring conformation.

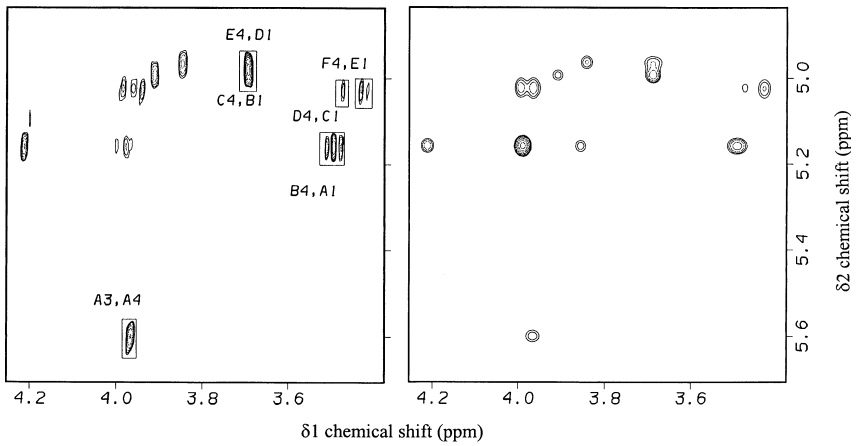

Figure 2 Hexasaccharide NOESY spectra

Two NOESY spectra are shown for the hexasaccharide. Left panel: experimental ^{1}H NOESY data accumulated at 600 MHz with a mixing time of 500 ms. Right panel: an IRMA back-calculated ^{1}H NOESY spectrum of the same spectral region. The residual water resonance is absent from the calculated spectrum.

Table 1 Experimental and theoretical coupling constants

Theoretical values were taken from Ferro et al. [15,17].

	$^3J_{1,2}$ (Hz)	$^3J_{2,3}$ (Hz)	$^3J_{3,4}$ (Hz)	$^3J_{4,5}$ (Hz)
$^1H_2$	3.2	2.1	4.7	–
$^2H_1$	8.3	7.7	2.8	–
$^1C_4$	1.8	2.6	2.6	1.3
$^2S_0$	6.3	9.5	9.3	2.8
A_{ring}exp*	3.1	–	4.7	–
C_{ring}exp†	3.2	5.8	3.6	–
E_{ring}exp†	3.2	5.6	3.9	–

* Calculated contribution of $^1H_2$ form: 100%.
† Calculated contribution of $^1C_4$ form: 69%.

Uronate residues, in contrast, have been found in various ring forms, and their conformation and flexibility in heparin have been the subject of a number of studies [15,17,43,47–49]. Here the hexasaccharide contains two different types of uronate residue, a presumably more rigid, 4,5-unsaturated uronate (ring A) at the non-reducing end and two 2-sulphated α-L-idopyranosyluronates (referred to as iduronates) (rings C and E). Uronate ring A, with co-planar C3, C4, C5 and O5 atoms, can exist in two different half-chair conformations, $^2H_1$ and $^1H_2$ (Scheme 1), differentiated by above-plane and below-plane positions for C1 and C2 atoms. The $^2H_1$ conformer with C2 lying above this plane shows a $^3J_{1,2}$ coupling constant greater than 6 Hz, whereas the $^1H_2$ conformation with C1 lying above this plane shows $^3J_{1,2}$ and $^3J_{2,3}$ coupling constants of less than 4 Hz. In this hexasaccharide observed values of 3.1 Hz for $^3J_{1,2}$ and 4.7 for $^3J_{3,4}$ are consistent with a preferred $^1H_2$ half-chair conformation (Table 1).

For internal iduronate rings C and E, $^3J_{2,3}$and $^3J_{3,4}$ coupling constants of 5.6–5.8 Hz and 3.6–3.9 Hz respectively indicate the presence of both $^1C_4$ chair and $^2S_0$ twisted-boat conformers (Scheme 1 and Table 1). Ferro et al. [15,17] have investigated the conformation of α-L-iduronate in various monosaccharides and oligosaccharides and suggested that when α-L-idopyranosyluronate and 2-*O*-sulpho-α-L-idopyranosyluronate residues are in an oligosaccharide sequence, only the $^1C_4$ and $^2S_0$ conformers are present at equilibrium (Scheme 1). The X-ray crystal structure of this hexasaccharide bound to FGF [22] shows ring C (having a tightly interacting 2-*O*-sulpho group) to be in the $^1C_4$ conformation, whereas ring E (weakly interacting with FGF) is in the $^2S_0$ conformation. In the solution structure the relative populations were calculated on the basis of iduronate coupling constants [15,17] in this hexasaccharide as $^1C_4$:$^2S_0$ = 69:31. Unfortunately, a potential NOE between H2 and H5, characteristic of the $^2S_0$ form, was obscured by the water resonance. In the heparin tetrasaccharide, however, this NOE was observed, and the H2–H5 interaction giving rise to this NOE was sufficient to drive the internal iduronate into this twisted boat conformation during conformational modelling [24]. In the hexasaccharide, discriminating iduronate H1–H2, H2–H3 and H3–H4 NOEs do show smaller distance violations in the twisted boat form. However, the initial $^1C_4$:$^2S_0$ distribution of 50:50 remains unchanged in the presence of the interactions giving rise to these intra-residue NOEs, suggesting that this distribution, which is consistent with the observed coupling constants, is realistic. Small deviations in expected coupling constants and NOEs in the hexasaccharide, however, might indicate a minor contribution from other ring forms that co-exist in equilibrium. In both rings, a slight twist at C2 and C3 carbons brings all substituents (except the C1 glycosidic oxygen) into equatorial positions thereby minimizing unfavourable 1,3 proton–proton steric interactions expected for flag-pole positions in the $^1C_4$ chair form. The conformation of iduronate in parent heparin and in dermatan sulphate has likewise been suggested to exist in a slightly distorted (C2 and C3 positions) $^1C_4$ chair conformation [17,47,50]. Conformational equilibria of the α-L-idopyranosyl uronate have been found to depend on its substituents as well as on those from adjacent residues [15,17,47–49].

Because iduronate residues C and E exist in equilibrium between $^1C_4$ and $^2S_0$ forms, conformational modelling was performed with both forms. This resulted in the use of four different initial structures in IRMA calculations. For glucosamines, the conformation of 6-*O*-sulphate groups was placed as the *gg* rotomer, and the H2–C2–N–H dihedral angle was fixed in the *trans* state [39]. Resulting structures were then subjected to an *in vacuo* NOE-restrained energy minimization procedure described in the Methods section. *R*-factors are listed in Table 2. With the exception of the terminal AB ($^1H_2$–$^4C_1$) linkage, RMS

Table 2 Calculated *R*-factors

R-factors were calculated for 32 NOE cross-peaks at five mixing times in accordance with eqn. (1). Restrained minimization in explicit solvent was used as described in the Methods section. Minimization was done in explicit solvent.

	IRMA *in vacuo*				Explicit solvent simulations	
Protocol	$K_{dis} = 3$	$K_{dis} = 15$	$K_{dis} = 30$	$K_{dis} = 60$	Restrained minimization	Minimization
All NOEs	0.4	0.38	0.31	0.25	0.25	0.4
Inter-residue NOEs	0.45	0.41	0.38	0.35	0.36	0.57

Table 3 Glycosidic dihedral angles and standard errors for different refinement protocols

Glycosidic dihedral angles are based on averages as described in the Results and discussion section. Letters below these values for md2 to md4 protocols specify the glycosidic linkage for which they were calculated. The original protocol was based on a structure reported by Mulloy et al. [38].

	Dihedral angle (°)									
Linkage ...	ΔUA2S(1→4)-α-D-GlcN*p*S6S		α-L-IdoAp2S(1→4)-α-D-GlcN*p*S6S				α-D-GlcNpS6S(1→4)-α-L-IdoA*p*2S			
Conformer ...	$^1H_2$-$^4C_1$		$^1C_4$-$^4C_1$		$^2S_0$-$^4C_1$		$^4C_1$-$^1C_4$		$^4C_1$-$^2S_0$	
Protocol	φ	ψ	φ	ψ	φ	ψ	φ	ψ	φ	ψ
Original	41	14	41	14	61	14	−39	−33	−9	−41
IRMA, $K_{dis} = 3$	65 ± 1	17 ± 1	51 ± 2	5 ± 6	74 ± 4	1 ± 4	−41 ± 1	−21 ± 1	−47 ± 1	−36 ± 2
IRMA, $K_{dis} = 15$	41 ± 1	27 ± 1	53 ± 1	−1 ± 10	80(56)*	1(−12)	−42 ± 1	−22 ± 1	45 ± 1	36 ± 3
IRMA, $K_{dis} = 30$	28 ± 2	33 ± 1	52 ± 1	−1 ± 9	83(48)	1(−11)	−41 ± 2	−23 ± 3	−44 ± 1	−36 ± 3
IRMA, $K_{dis} = 60$	30 ± 1	43 ± 1	54 ± 1	12 ± 3	81(47)	2(−9)	−41 ± 2	−23 ± 2	−42 ± 1	−35 ± 3
Eq. + restrained minimization in solvent	29 ± 13	48 ± 8	54 ± 1	12 ± 5	77(44)	18(−8)	−35 ± 4	−28 ± 5	−44 ± 4	−35 ± 4
Minimization in solvent	54 ± 17	35 ± 6	53 ± 1	8 ± 7	81(40)	22(−7)	−35 ± 4	−24 ± 6	−47 ± 5	−35 ± 3
md2	–	–	63 ± 6	26 ± 7	34 ± 9	−14 ± 9	–	–	−48 ± 7	−14 ± 8
			C–D	C–D	E–F	E–F			D–E	D–E
md3	–	–	54 ± 8	−43 ± 8	91 ± 7	28 ± 9	−25 ± 6	−26 ± 7	−56 ± 7	−41 ± 8
			E–F	E–F	C–D	C–D	D–E	D–E	B–C	B–C
md4	81 ± 7	25 ± 7	–	–	42 ± 8	−4 ± 8	–	–	−66 ± 7	−34 ± 9
	A–B	A–B			E–F	E–F			D–E	D–E

* Two different sets of dihedral values were found for C–D and E–F linkages; the latter are indicated in parentheses.

Table 4 Absolute average distance violations for inter-residue NOEs

Distance limits were calculated from experimental build-up curves during IRMA. Absolute values of distance violations were averaged over the ensemble of four structures obtained after restrained minimization in explicit solvent as described in the Materials and methods section.

	Violation (Å)				
i; *i*+1	$H^i_1 - H^{i+1}{}_3$	$H^i_1 - H^{i+1}{}_4$	$H^i_1 - H^{i+1}{}_5$	$H^i_1 - H^{i+1}{}_{6R}$	$H^i_1 - H^{i+1}{}_{6S}$
A–B	0.53	0.07	0.15	–*	0.07
B–C	0.06	0.06	–	–	–
C–D	–	0.06	–	0.04	–
D–E	0.03	0.04	–	–	–
E–F	–	0.04	–	0.04	–

* Direct NOE volume refinement was used for this peak, which overlapped with A1–A3.

values (Table 3) were obtained by averaging over four values for the same linkage located in two different positions in the hexasaccharide. For example, to calculate the average value for a glucosamine–iduronate $^4C_1$–$^1C_4$ linkage, four structures were used: two with ring C in the chair form (B–C linkage) and two with ring E in the chair form (D–E linkage). Therefore calculated RMS values indicate not only deviations within a single linkage but also contributions from different positions in the oligosaccharide.

To check the dependence of the overall structure on the strength of the restraint potential, this protocol was repeated with different distance restraint force constants of 12.5, 62.7, 125.5 and 251 J (3, 15, 30 and 60 kcal)/mol per Å². Most glycosidic torsion angles (Table 3) were not significantly modified by increasing the force constant, which indicates that this set of inter-residue NOEs allows dihedral angles to be relatively well defined. Increasing the force constant naturally led to improved *R*-factors (Table 2) primarily through small changes in intra-ring distances and minimal reorientations of 6-*O*-sulphate groups, which remained in the *gg* state for glucosamine rings B and D. In ring F, the 6-*O*-sulphate group was found to be *gt* when ring E was in the $^1C_4$ conformation or between *gg* and *gt* when ring E was in the $^2S_0$ conformation. The latter situation might be the result of the restraint energy and a large *gg*-to-*gt* transition energy barrier. Moreover, with the iduronate ring in the $^2S_0$ conformation, the use of larger force constants results in the formation of two distinct inter-residue orientations for C–D and E–F rings (Table 3). In this case, this might be the result of an

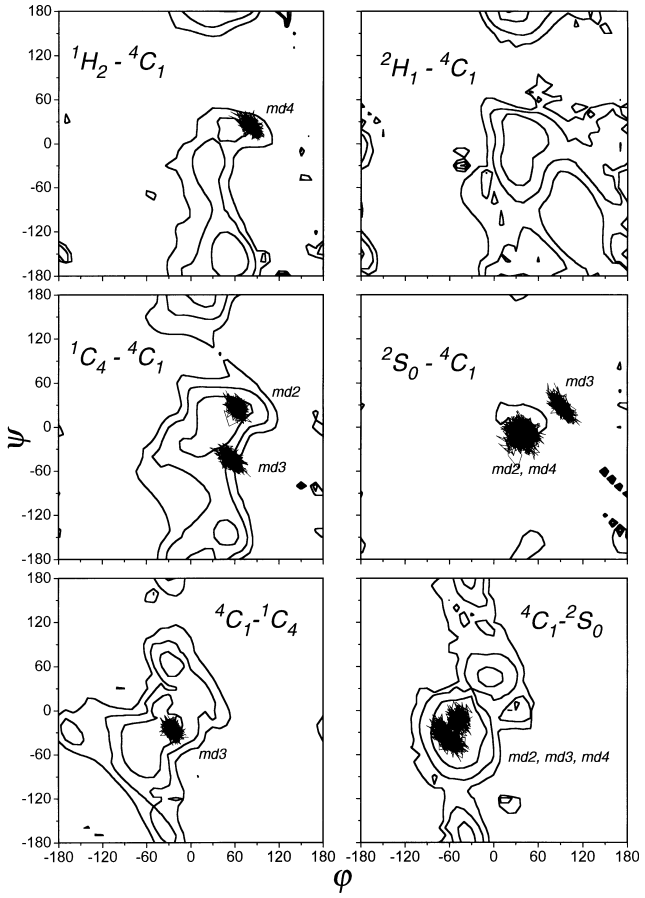

Figure 3 Potential-energy contour maps calculated for model disaccharides as described in the Methods section

Contour lines are shown for 8.4, 16.8 and 25.2 kJ/mol. Also shown are MD trajectories (sampling period from 100 to 600 ps) used to calculate average glycosidic dihedral angles listed in Table 3.

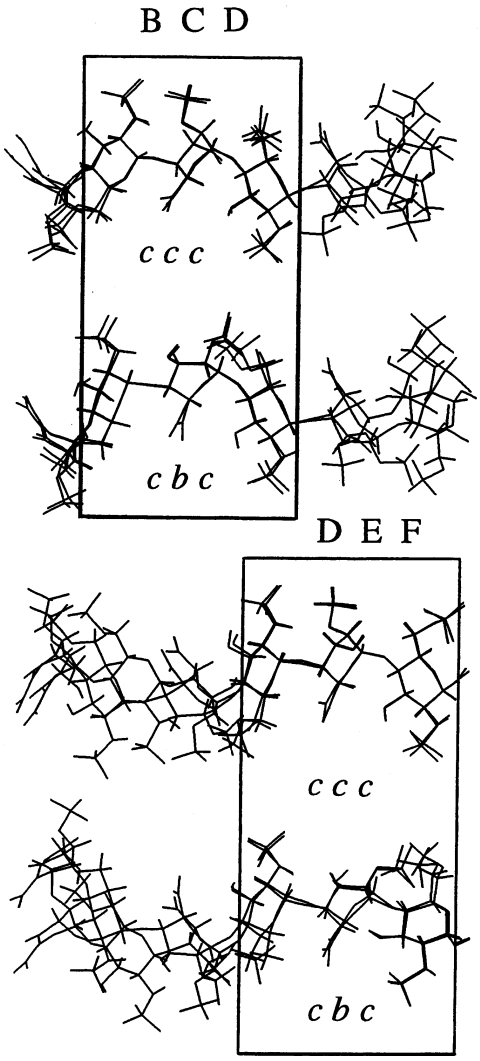

Figure 4 Superposition of IRMA-calculated structures

Because structural calculations were performed with both chair (*c*) and skewed boat (*b*) forms of internal iduronates, there are four sets of structures. The top two sets were generated by superposing rings B, C and D (boxed) for ring conformations *ccc* (top) and *cbc* (second from top) respectively. The bottom two sets were generated by superposing rings D, E and F (boxed) for ring conformations *ccc* (second from bottom) and *cbc* (bottom) respectively.

insufficient number of inter-residue NOEs. Alternative values for the E–F linkage correlate with a distorted orientation of the 6-*O*-sulphate group mentioned above. Because one of the two main NOEs observed across this glycosidic linkage is between E1 and F6R protons (Table 4), this intermediate orientation of the F-ring 6-*O*-sulphate group is probably associated with differences in inter-ring dihedral angles. The existence of two glycosidic conformations might also result from terminal effects in this relatively short oligosaccharide. In any event, a distance restraint force constant of 251 J (60 kcal)/mol per Å^2 was used in subsequent calculations.

Because the forcefield used here is different from that used by Mulloy et al. [39], conformational energy maps (Figure 3) were calculated (Biosym/MSI software) for each disaccharide pair in the molecule; φ and ψ torsional angles were varied over the full range of angles (-180 ° to $+180$ °), and structures were energy-minimized every 10 ° with a torsional restraint of 41 840 J (10 000 kcal)/rad^2 and the use of conjugate gradients until the RMS derivative was smaller than 0.01. A distance-dependent dielectric of 4*r* was used during *in vacuo* calculations. Although these energy maps provide only an estimate of the complicated glycosidic torsion energy surface in longer oligosaccharides in explicit solvent water [4], they can still be useful when considering 'virtual' conformers that result from using experimentally derived pseudo-energy restraint terms.

The need for computationally expensive explicit solvent simulations arises from the fact that the heparin-derived hexasaccharide is highly negatively charged. Further structural refinement was performed in the presence of solvent water molecules and sodium counterions. In this type of simulation, appropriate equilibration of the solvent box is crucial owing to the sensitivity of the potential energy function to the exact separation of ions and the dominance of solvent–solvent non-bonded energy terms in the total potential energy function [43]. Although such simulations have been performed with smaller and less charged saccharides [4,43,45], none have been done with this highly negatively charged heparin-derived hexasaccharide. *R*-factors remained essentially the same; however, somewhat modified conformations were produced owing to the presence of solvent. Moreover, some of the resulting conformations did not cor-

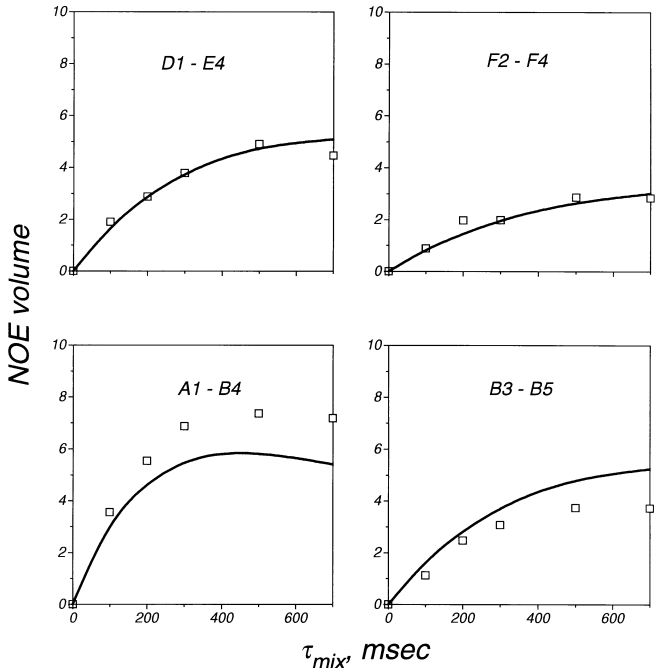

Figure 5 NOE build-up curves

Experimental and IRMA-calculated NOE build-up curves are shown for several inter-proton NOEs as indicated. Symbols represent experimentally determined NOEs, and lines give calculated build-up curves for the four structures calculated with the modelling protocol described in the text.

respond to the global energy minimum because of the presence of pseudo-energy restraint terms and the possibility of conformations being trapped within local minima. RMS values increased on the addition of explicit solvent (Table 3), possibly indicating the presence of local minima on the complicated energy surface that corresponds to the NOE-derived distance constraints. This probably provides a more realistic picture than 'precise' values for dihedral angles obtained from *in vacuo* calculations and reflects a certain degree of internal mobility around glycosidic bonds.

These IRMA-derived structures have been superposed (ring carbons and glycosidic oxygens) in Figure 4. Because structural calculations have been performed using both chair (*c*) and skewed boat (*b*) forms of internal iduronates, there are four sets of structures covering all combinations. The top two sets were generated by superposing rings B, C and D (boxed) for ring conformations *ccc* (top) and *cbc* (second from top) respectively. The bottom two sets were generated by superposing rings D, E and F (boxed) for ring conformations *ccc* (second from bottom) and *cbc* (bottom) respectively. RMS deviation (RMSD) values for superposed segments were all less than 0.35 Å. Regardless of the iduronate ring conformation, all structures shown here, along with their glycosidic angles reported in Table 3, define an extended heparin conformation with a right-handed twist to the inter-ring conformation with all sulphates extending equatorially. The heparin-derived tetrasaccharide structure [24] was also refined here by using the current force field and previously reported experimental data. Superposition of tetrasaccharide rings B, C and D with hexasaccharide rings D, E ($^3S_0$) and F gave an RMSD value of 0.5 Å, indicating a rather good consistency in glycosidic conformations for these two oligosaccharides of different lengths.

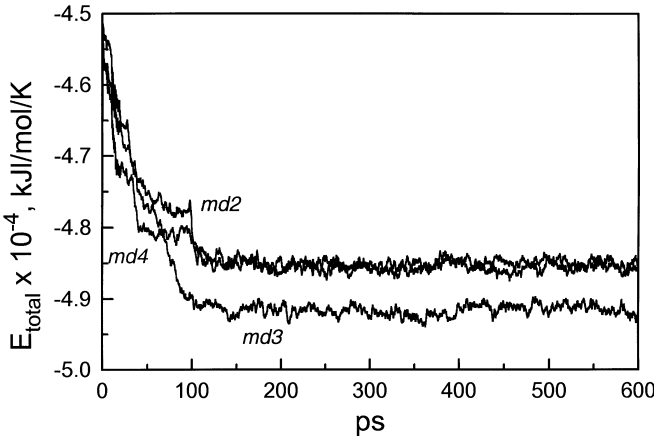

Figure 6 Total energy of the simulated system plotted against simulation time for different MD runs

To check that this ensemble of structures is realistic, NOESY spectra were back-calculated and found to compare favourably with experimental data. One portion from this back-calculated NOESY is shown in Figure 2 (right panel). In addition, Figure 5 exemplifies how well NOE build-up curves are approximated with this ensemble of structures. Here one can see that the use of an average leakage rate of 0.1 s^{-1} (see the Methods section) cannot adequately describe all experimental NOEs at longer mixing times. These deviations, however, are minimal in terms of actual distances owing to weighting by the inverse sixth power of the internuclear distance. NOE-distance violations are listed in Table 4. Even though most violations are minimal, those for A1–B3 and A1–B5, which help define the glycosidic angles of the AB linkage, are rather large. Increasing the force constant in IRMA calculations also distorts dihedral angles for the AB linkage. To test the sensitivity of NMR data on structural parameters, IRMA-derived restraints were removed as described in the Methods section, which led to increased *R*-factors (Table 2). Minimized structures showed the largest change at the AB linkage, consistent with relaxing strain introduced by A1–B3 and A1–B5 NOE restraints (Table 4). Other glycosidic linkages did not change significantly. For all four structures, restraint forces introduced most strain in valence angles and less in bond lengths and torsional angles. Regardless of the dominance of solvent–solvent non-bonded energy terms, energy differences with and without restraints were negligible compared with the total potential energy.

To achieve a better evaluation of the stability of these conformations, long-timescale (600 ps) unrestrained MD runs were performed on the four structures in explicit solvent. Although a complete analysis would require information on the dynamical behaviour of glycosidic dihedral angles, side chains and ring conformations, only the first two can be adequately sampled during the 600 ps simulation time. Side-chain motions were determined by the following changes in dihedral angles: 2-*O*-sulphate by H^2–C^2–O–S; 2-*N*-sulphate by H^2–C^2–N–H and 6-*O*-sulphate by O^5–C^5–C^6–O^6 angles. Pyranose ring conformations were measured by using the Cremer–Pople ring-puckering formalism ([51], and Figure 1 in [43]) which reduces Cartesian coordinates to a set of three parameters: Q, φ and θ, which can be measured along the MD trajectory. The time dependences of the Cremer–Pople θ sugar-pucker angle for simulations 2–4 are shown in Figure 6. For reference, MD simulations are numbered

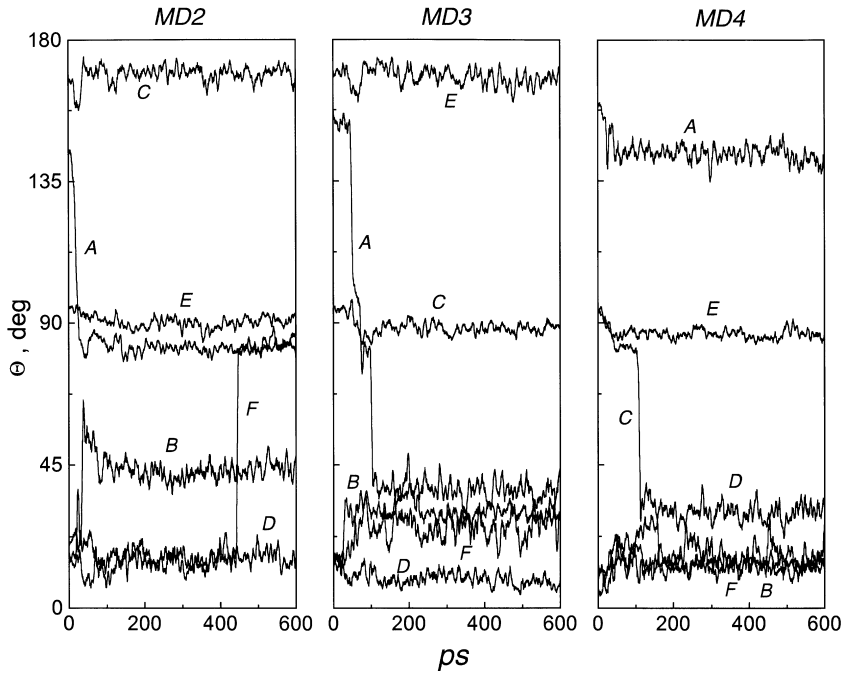

Figure 7 Sugar pucker θ angle plotted against the simulation time for different MD runs

Lines connect averages over 5 ps. Letters denote different rings. θ angles for ideal chair and boat conformations of the pyranose ring are: $^1C_4$, 180°; $^4C_1$, 0°; various boat forms, 90°. Precise boat and half-chair forms are defined by the ϕ angle [42].

md1 to md4 on the basis of initial internal iduronate conformations, *cc*, *cb*, *bc* and *bb* respectively, where *c* stands for $^1C_4$ chair and *b* stands for $^2S_0$ skewed boat. Although the total energy of the system remained relatively stable during the last 500 ps (Figure 7), significant decreases during the first 100 ps were accompanied by both solvent relaxation and changes in glycosidic and side-chain torsion angles. Solvent relaxation occurred rapidly, whereas slower relaxation processes involved ring and side-chain reorientations, which can result in anomalous ring conformations owing to large electrostatic energy contributions. Because such ring distortions were observed in md1, only MD simulations on structures md2, md3 and md4 were used to assess structural stability with this approach. Some trajectories, moreover, resulted in the formation of alternative iduronate and uronate ring conformations (Figure 6); these, too, were not used. Average values and standard deviations for glycosidic torsion angles in the accepted structures are listed in Table 3. Dynamics trajectories are also plotted on the energy maps in Figure 4, where, for most glycosidic angles, orientations fall within the low-energy regions obtained for model disaccharides.

Comparison of these average parameters with NMR-derived values shows that C–D and E–F inter-ring orientations remain quite stable, whereas rather large changes in the φ angle of the A–B linkage are observed. The use of strong inter-residue NOEs (A1–B3 and A1–B5) during *in vacuo* protocols resulted in a distortion of the A–B linkage that was not relieved during initial MD protocols with explicit solvent. This torsional angle relaxation apparently occurs only during unrestrained MD runs. Furthermore, large changes in the Ψ glycosidic angle occurred at the terminal E–F linkage in md3 soon after releasing solute positional restraints during the equilibration period. Although there is no visible ring distortion associated with this transition, the mobility of the 6-*O*-sulphate group increased significantly. This new conformation might correspond to a lower-energy minimum as suggested by its subsequent stability during the final 500 ps of sampling. In general, side-chains, as expected, were found to be more mobile than rings and glycosidic angles. After equilibration, several transitions were observed in the smaller glucosamine 2-*N*-sulphates. Most of the time, these groups remained in the *trans* conformation (H^2–C^2–N–H angle approx. 180°) in agreement with the measured $^3J_{NH,CH_2}$ value of 9.4 Hz. Internal ring 6-*O*-sulphates were stable in the *gg* orientation. The alternative 6-*O*-sulphate *tg* orientation (found to be a negligible contribution in the heparin-derived tetrasaccharide conformation [24]) in ring B of md3 could be caused by a conformational transition in adjacent ring A. For terminal ring F, both *gt* and *gg* orientations were present, which also agrees with our previous tetrasaccharide study. Lastly, 2-*O*-sulphate groups were found to be in the *cis* orientation, in agreement with the results of Ragazzi et al. [52]. Thus if MD simulations are performed in explicit solvent a better sampling of the complicated energy surface is provided; this is reflected in the presence of decreased *R*-factors compared with unrestrained minimizations (Table 2).

It is also important to note that the existence of different ring conformations did not change the overall shape of the hexasaccharide. As pointed out by Ferro et al. [15], the highest RMS is for the flexible residue itself, whereas the RMS values for flanking residues are quite low. Thus the use of the 'correct' conformational populations, close to those obtained from coupling constants, is important in deriving correct inter-proton distances within the same ring and less important in deriving inter-proton distances between flexible and more rigid residues. The latter defines the overall structure of the saccharide. The values derived for the hexasaccharide (Table 3) give a right-handed sense to the overall conformation. Values for these glycosidic angles differ from those reported by Mulloy et al. [39]

by up to 30°. However, the authors of that paper used a preparation of heterogeneous heparin yielding NOEs that would also be averaged over different size fragments and making derived conformations less accurate than those determined with well-characterized homogeneous heparin fragments in the current study. Additionally, differences in glycosidic angles might also be attributed to the use of different force fields, i.e. MM2 compared with Amber in our case. These new conformations, however, remained in a low-energy region on the basis of model disaccharide potential energy calculations. The current force field gives very broad low energy regions from which it is hard to get reliable torsion angles. Combining energy calculations with experimentally derived restraints helps to limit acceptable glycosidic torsion angles. The addition of explicit solvent makes the problem of finding the best 'virtual' minimum more complicated. This is reflected by higher standard errors found for average dihedral angles. At the same time these higher errors might indicate flexibility about glycosidic bonds [38,53].

Further refinement of carbohydrate conformational parameters can be achieved either by implementing more sophisticated IRMA models that will consider the effects of anisotropic tumbling, internal mobility and different leakage rates [54–56] or by using more sophisticated simulation protocols that include long-range explicit solvent MD. The latter approach was used here. MD simulations provide better sampling of the complex potential energy surface and test the stability of conformational parameters obtained during the early stages of structure refinement. Such simulations, however, should be approached with caution owing to significant contributions from electrostatic interactions that make the MD simulation quite sensitive to initial positions of counterions as well as to initial solute conformations. Equilibrating the solution with restrained solute partly removes the first problem by allowing the surrounding solvent and counterions to relax. Use of the NMR-derived conformation as a starting point, even though it is still rather far from the global minimum owing to limited or inaccurate experimental information, can cause problems during MD equilibrations when solute positional restraints are gradually removed. For example, ring distortions are often coupled to reorientations of side chains that, being bulky and highly charged, tend to distort the surrounding solvent and modify the electrostatic component of the total energy of the system. A more rigorous method such as the Particle Mesh Ewald approach [57,58] has provided better results with analogous highly charged DNA oligonucleotides. Such simulations can provide a better understanding of oligosaccharide structure and dynamics. In addition to the drawbacks associated with a complicated explicit-solvent system, limitations are introduced by the force field. Even though the Amber force field has proved itself in protein dynamics simulations, the more sophisticated CVFF and CFF91 force fields [59], which include cross-energy terms absent from Amber, usually perform better in carbohydrate simulations. Our use of Amber was dictated by the availability of sulphate parameters derived for this force field from calculations *ab initio*. To our knowledge, sulphate parameters have not been generated for MD simulations in explicit solvent.

After conformational refinement, NMR-derived solution structures were compared with the X-ray crystal structure of the hexasaccharide bound to the protein FGF [22]. Interestingly, when bound to FGF, hexasaccharide glucosamine rings remain in the stable $^4C_1$ chair form as in solution, whereas iduronates are found in one of their preferred ring conformations or the other, i.e. $^1C_4$ chair (ring C) or $^2S_0$ skewed boat (ring E). In solution, iduronates interconvert between these two ring conformations. For more detailed differences between bound and free hexasaccharide conformations, glycosidic angles were compared. For this, only the NMR-derived structure with iduronate rings C and E in chair and boat forms respectively was chosen because the bound structure has the same two iduronate ring conformations. φ, Ψ glycosidic angles are listed in Table 5. Note that in the high-affinity site in bound hexasaccharide (residues A, B, C, D) [22], glycosidic angles are considerably different from those in the solution free state (30° to 40° different in some instances), whereas glycosidic angles in the low-affinity site (residues D, E, F) [22] are all nearly within 10° of each other. There is greater change in glycosidic angles at residues in the high-affinity FGF-binding site. RMS differences between structures show a similar trend. Superposition of ring atoms in residues D, E and F give a 0.41 Å RMSD, whereas superposition of ring atoms in residues A, B, C and D give a 0.85 Å RMSD.

Table 5 Glycosidic angles in bound and free hexasaccharide

	Bound		Free	
Angle	φ (°)	ψ (°)	φ (°)	ψ (°)
AB	61	13	18	58
BC	−25	−1	−33	−32
CD	50	25	54	19
DE	−42	−40	−49	−31
EF	49	22	43	12

Conclusions

To understand the basis for heparin activity in biological systems, it is most important to have as detailed a knowledge as possible about the structure of heparin and the role of various functional groups in heparin. The present study was aimed at determining the conformational properties of a small homogeneous fragment of heparin by using a combination of experimental (NMR) and molecular modelling techniques. Such heparin fragments can be viewed as basic building blocks for the native glycosaminoglycan, and structural information obtained on the hexasaccharide can be used to model longer heparin chains. Present results on the hexasaccharide have shown that the overall folding places sulphate and carboxylate side groups at the edges of the structure, which displays a slight right-handed twist. All glucosamine rings are stable in the $^4C_1$ chair conformation, whereas iduronate rings interconvert between chair and skewed boat forms. When bound to the protein FGF, this hexasaccharide also has glucosamines in the chair conformation, whereas one iduronate is in the $^1C_4$ chair and the other is in the $^2S_0$ skewed boat. This indicates that iduronate rings, flexible in solution, can be locked into either conformation when protein bound. Such conformational information might be used to rationalize the interactions of heparin with various biological targets and to assist in the design of pharmaceutical agents.

This work was supported by grants from the American Heart Association (AHA-96006050) and the National Institutes of Health (GM38060) and benefited from use of the high-field NMR facility at the University of Minnesota (Minneapolis, MN, U.S.A.).

REFERENCES

1 Jeanloz, R. W. (1975) Adv. Exp. Med. Biol. **52**, 3–12
2 Lindahl, U. (1974) Int. Rev. Sci., Org. Chem. Ser. **2** (7), 283–289
3 Perlin, A. S., Mackie, D. M. and Dietrich, C. P. (1971) Carbohydr. Res. **18**, 185–192

4 Homans, S. W. and Forster, M. (1992) Glycobiology **2** (2), 143–151
5 Tvaroska, I., Hricovani, M. and Petrakova, E. (1989) Carbohydr. Res. **189**, 359–362
6 Bruyn, A. (1991) J. Carbohydr. Chem. **10** (2), 159–180
7 Cumming, D. A. and Carver, J. P. (1987) Biochemistry **26**, 6664–6676
8 Merchant, Z. M., Kim, Y. S., Rice, K. G. and Linhardt, R. J. (1985) Biochem. J. **229**, 369–377
9 Linker, A. and Hovingh, P. (1984) Carbohydr. Res. **127**, 75–94
10 Pervin, A., Gallo, C., Jandik, K., Han, X.-J. and Linhardt, R. J. (1995) Glycobiology **5**, 83–95
11 Gettins, P. and Horne, A. (1992) Carbohydr. Res. **223**, 81–98
12 Horne, A. and Gettings, P. (1992) Carbohydr. Res. **225**, 43–57
13 Ragazzi, M., Ferro, D. R., Provasoli, A., Pumilia, P., Cassinari, A., Torri, G., Guerrini, M., Casu, B., Nader, H. B. and Dietrich, C. P. (1993) J. Carbohydr. Chem. **12**, 523–535
14 Gould, S. E. B., Gould, R. O., Rees, D. A. and Wight, A. W. (1975) J. Chem. Soc., Perkin Trans. II, 392–399
15 Ferro, D. R., Provasolli, A., Ragazzi, M., Torri, G., Casu, B., Gatti, G., Jacquinet, J. C., Sinay, P., Petitou, M. and Choay, J. (1986) J. Am. Chem. Soc. **108**, 6773–6778
16 Desai, U. R., Wang, H. M., Kelly, T. R. and Linhardt, R. J. (1993) Carbohydr. Res. **241**, 249–259
17 Ferro, D. R., Provasolli, A., Ragazzi, M., Casu, B., Torri, G., Bossennec, V., Perty, B., Sinay, P., Petitou, M. and Choay, J. (1990) Carbohydr. Res. **195**, 157–167
18 Tyrrell, D. J., Ishihara, M., Rao, N., Horne, A., Kiefer, M. C., Stauber, G. B., Lam, L. H. and Stack, R. J. (1993) J. Biol. Chem. **268**, 4684–4689
19 Maccarana, M., Casu, B. and Lindahl, U. (1993) J. Biol. Chem. **268**, 23898–23905
20 Habuchi, H., Suzuki, S., Saito, T., Tamura, T., Harada, T., Yoshida, K. and Kimata, K. (1992) Biochem. J. **285**, 805–813
21 Turnbull, J. E., Fernig, D. G., Ke, Y., Wilkinson, M. C. and Gallagher, J. T. (1992) J. Biol. Chem. **267**, 10337–10341
22 Fahem, S., Hileman, R. E., Fromm, J. R., Linhardt, R. J. and Rees, D. C. (1996) Science **271**, 1116–1120
23 Lyon, M., Deakin, J. A., Mizuno, K., Nakamura, T. and Gallagher, J. T. (1994) J. Biol. Chem. **269**, 1216–11223
24 Mikhailov, D., Mayo, K. H., Vlahov, I. R., Toida, T., Pervin, A. and Linhardt, R. J. (1996) Biochem. J. **318**, 93–102
25 Linhardt, R. J., Rice, K. G., Kim, Y. S., Lohse, D. L., Wang, H. M. and Loganathan, D. (1988) Biochem. J. **254**, 781–787
26 Loganathan, D., Wang, H. M., Mallis, L. M. and Linhardt, R. J. (1990) Biochemistry **29**, 4362–4368
27 Bax, A. and Davis, D. G. (1985) J. Magn. Reson. **65**, 355–360
28 Jeener, J., Meier, B., Backman, P. and Ernst, R. R. (1979) J. Chem. Phys. **71**, 4546–4550
29 Wider, G., Macura, S., Anil-Kumar, X. X., Ernst, R. R. and Wüthrich, K. (1984) J. Magn. Reson. **56**, 207–234
30 States, D. J., Haberkorn, R. A. and Ruben, D. J. (1982) J. Magn. Reson. **48**, 286–293
31 Marion, D. and Wüthrich, K. (1983) Biochem. Biophys. Res. Commun. **113**, 967–975
32 Wüthrich, K. (1986) NMR of Proteins and Nucleic Acids, Wiley-Interscience, New York
33 Homans, S. W. (1990) Biochemistry **29**, 9110–9118
34 Huige, C. J. M. and Altona, C. (1995) J. Comput Chem. **16** (1), 56–79
35 Glennon, T. M., Zheng, Y.-J., Grand, S. M., Shutzberg, B. A. and Merz, Jr., K. M. (1994) J. Comput Chem. **15** (9), 1019–1040
36 Boelens, R., Koning, T. M. G. and Kaptein, R. (1988) J. Mol. Struct. **173**, 299–311
37 Boelens, R., Koning, T. M. G., van der Marel, G. A., van Boom, J. H. and Kaptein, R. (1989) J. Magn. Reson. **82**, 290–308
38 Hricovini, M. and Torri, G. (1995) Carbohydr. Res. **268**, 159–175
39 Mulloy, B., Forster, M. J., Jones, C. and Davies, D. B. (1993) Biochem. J. **293**, 849–857
40 Yip, P. F. (1993) J. Biomol. NMR **3**, 361–365
41 Haasnoot, C. A. G., de Leeuw, F. A. A. M. and Altona, C. (1980) Tetrahedron **36**, 2783–2792
42 Gonzales, C., Rullmann, J. A. C., Bonvin, A. M. J. J., Boelens, R. and Kaptein, R. (1991) J. Magn. Reson. **91**, 659–664
43 Forster, M. and Mulloy, B. (1993) Biopolymers **33**, 575–588
44 Cheetham, N. W. H. and Lam, K. (1996) Carbohydr. Res. **282**, 13–23
45 Ott, K.-H. and Meyer, B. (1996) Carbohydr. Res. (1996) **281**, 11–34
46 Casu, B. (1985) Adv. Carbohydr. Chem. Biochem. **43**, 51–60
47 Torri, G., Casu, B., Gatti, G., Petitou, M., Choay, J., Jacquine, J. C. and Sinay, P. (1985) Biochem. Biophys. Res. Commun. **128**, 134–140
48 Huckerby, N. T. and Nieduszynski, A. I. (1982) Carbohydr. Res. **103**, 141–145
49 Huckerby, N. T., Senderson, P. N. and Nieduszynski, A. I. (1985) Carbohydr. Res. **138**, 199–206
50 Gatti, G., Casu, B., Torri, G. and Vercellotti, J. R. (1979) Carbohydr. Res. **68**, C3–C7
51 Cremer, D. and Pople, J. A. (1975) J. Am. Chem. Soc. **97**, 1354–1358
52 Ragazzi, M., Ferro, D. R. and Provasoli, A. (1986) J. Comp. Chem. **7** (2), 105–112
53 Hricovini, M., Tvaroska, I. and Hirsch, J. (1990) Carbohydr. Res. **198**, 193–203
54 Zhu, L. and Reid, B. R. (1995) J. Magn. Reson. B **106**, 227–235
55 Leeflang, B. R. and Kroon-Batenburg, L. M. J. (1992) J. Biomol. NMR **2**, 495–518
56 Kroon-Batenburg, L. M. J., Kroon, J., Leeflang, B. R. and Vliegenthart, J. F. G. (1993) Carbohydr. Res. **245**, 21–42
57 Darden, T. A., York, D. and Pedersen, L. G. (1993) J. Chem. Phys. **98**, 10089–10092
58 Cheatham, D. and Kollman, P. (1996) J. Mol. Biol. **259**, 434–444
59 Asensio, J. L., Martin-Pastor, M. and Jiminez-Barbero, J. (1995) Int. J. Biol. Macromol. **17**, 137–148

Received 14 March 1997/12 June 1997; accepted 7 July 1997